

Spring warming drives past and future shifts in Great Plains storm intensity

Chijun Sun (✉ chijunsun@utexas.edu)

University of Texas at Austin <https://orcid.org/0000-0002-3668-346X>

Timothy Shanahan

University of Texas at Austin

Pedro DiNezio

University of Colorado Boulder

Nicholas McKay

Northern Arizona University <https://orcid.org/0000-0003-3598-5113>

Priyadarsi Roy

Universidad Nacional Autonoma de Mexico

Article

Keywords: Great Plains, storm intensity, spring warming

Posted Date: October 12th, 2020

DOI: <https://doi.org/10.21203/rs.3.rs-76477/v1>

License:  This work is licensed under a Creative Commons Attribution 4.0 International License.

[Read Full License](#)

Version of Record: A version of this preprint was published at Nature Geoscience on November 29th, 2021. See the published version at <https://doi.org/10.1038/s41561-021-00860-8>.

1
2
3
4
5
6
7
8
9
10
11
12
13
14
15
16

Spring warming drives past and future shifts in Great Plains storm intensity

Chijun Sun^{1*}, Timothy M. Shanahan¹, Pedro N. DiNezio^{2,3}, Nicholas P. McKay⁴, Priyadarsi Roy⁵

Affiliations:

¹Department of Geological Sciences, The University of Texas at Austin, Austin, TX 78712, USA.

²Institute for Geophysics, The University of Texas at Austin, Austin, TX 78758, USA.

³Atmospheric and Oceanic Sciences, University of Colorado Boulder, Boulder, CO 80309, USA.

⁴School of Earth and Sustainability, Northern Arizona University, Flagstaff, AZ 86011, USA

⁵Instituto de Geología, Universidad Nacional Autónoma de México, Ciudad Universitaria, Ciudad de México CP 04510, Mexico.

*Correspondence to: Email: chijunsun@utexas.edu

17 **Abstract:**

18

19 The climate of the Great Plains is dominated by mesoscale convective systems (MCS), which
20 supply a significant portion of warm season rainfall and are responsible for severe weather and
21 flooding across the region. However, little is known about past behavior and long-term drivers
22 of these systems, limiting our ability to predict future changes in hydroclimate and extreme
23 weather for much of the central US. Here, we generate a new record of past MCS activity and
24 hydroclimate variability from central Texas and compare it against the results of transient
25 climate model simulations to understand the underlying causes of past changes in extreme
26 weather and climate in the central US. We find that changes in storm activity and hydroclimate
27 in the southern Great Plains over the last the 20,000 years were dominated by changes in the
28 strength of the Great Plains Low Level Jet, driven by springtime land surface temperature
29 changes. These results suggest that a similar dynamical response to future warming will lead to
30 enhanced MCS activity and an increase in extreme weather and flooding across the southern and
31 central Great Plains in the future.

32

33

34 Much of the rainfall over the central United States (U.S.) is generated by mesoscale convective
35 systems (MCS), large (>100 km) organized convective storms ¹ that produce intense
36 precipitation and are often accompanied by flooding, hail and damaging winds. Economic losses
37 due to convective storms in the U.S. exceed U.S. \$10 billion annually ², the majority of which is
38 associated with MCSs ³. Over the past few decades, the frequency and intensity of central U.S.
39 MCSs has increased dramatically ⁴, far beyond the predicted rate of increase in precipitable
40 water (~7% per °C warming) based on the thermodynamic Clausius-Clapeyron relationship.
41 Instead, this trend has been attributed to a strengthening southerly low-level flow and the
42 associated Great Plains low-level jet (LLJ), which provides the moisture and energy required for
43 MCS development ⁴. Simulations of future warming with global general circulation models
44 predict a strengthening of the LLJ in response to continued surface warming of the eastern
45 Rockies and western Great Plains, but there is little consensus about the associated changes in
46 MCS development and precipitation ⁵⁻⁹, leading to large uncertainties in the potential risks of
47 future drought, floods and extreme storms⁶⁻⁸.

48
49 To improve our understanding of the sensitivity of Great Plains hydroclimate and extreme
50 rainfall to climate change, we generated a new multiproxy reconstruction of changes in MCS
51 activity and vegetation in the southern Great Plains from the sediments of Hall's Cave, Texas
52 (30°8'11''N, 99°32'6''W). This region is amongst the most poorly studied in North America,
53 with few continuous, well-dated and high-resolution paleoclimate records. Hall's Cave is an
54 exception: 37 radiocarbon dates provide a robust, linear age-depth model spanning the past
55 20,000 years (Supplementary Information), during which large shifts of global climate since the
56 Last Glacial Maximum (LGM) are ideal testbeds to assess the controls on Great Plains MCS

57 activity and hydroclimate. Furthermore, the site is uniquely sensitive to changes in hydroclimate
58 and MCS activity; nearly 70% of the warm season precipitation is derived from MCS storms ¹,
59 and the site is located on a steep hydroclimatic and ecological gradient between the southwestern
60 subtropical grasslands and the temperate forests of the southeast U.S.

61

62 Here, we use a multiproxy approach to simultaneously reconstruct past changes in MCS activity,
63 climate and associated vegetation changes. First, we use the hydrogen isotope composition of
64 sedimentary plant waxes (δD_{wax}) as a proxy for MCS-driven rainfall activity. This interpretation
65 is based on observations of modern precipitation over central Texas, which demonstrates that the
66 stable isotopic composition of rainfall is largely controlled by changes in MCS activity rather
67 than precipitation amount ¹⁰. These isotopic changes are preserved in sedimentary plant waxes
68 (δD_{wax}), providing a proxy record of past changes in MCS activity¹¹ (see Supplementary
69 Information for details). Our interpretation of δD_{wax} is supported by changes in %Ti, which
70 reflects enhanced erosion of terrigenous sediment into the cave during extreme rainfall events.
71 Hall's Cave consists of a single room with an upslope opening that permits sediment to be
72 washed into the cave during rainstorms. Although the sediment stratigraphy is likely complex
73 near the cave entrance, our sampling location deeper in the cave receives terrigenous material
74 only during events associated with extreme storms.

75

76 Finally, we reconstruct past vegetation changes from carbon isotopic composition of bulk
77 sedimentary organic matter ($\delta^{13}\text{C}_{\text{OM}}$), which we interpret as reflecting changes in hydroclimate
78 based on modern vegetation-climate relationships. Plants using the C₄ photosynthetic pathway
79 have higher water use efficiency, higher $\delta^{13}\text{C}$ values (-9 to -14‰) and are characteristic of

80 savannas and semi-arid grasslands, whereas C₃ plants have lower $\delta^{13}\text{C}$ values (-25 to -29‰),
81 including most woody shrubs, trees and winter grasses, and are associated with cooler and wetter
82 environments¹². Thus, $\delta^{13}\text{C}_{\text{OM}}$ values provide a record of landscape-scale vegetation cover
83 associated with past changes in hydroclimate.

84

85 The $\delta\text{D}_{\text{wax}}$, %Ti and $\delta^{13}\text{C}_{\text{OM}}$ records from Hall's Cave show remarkably coherent changes over
86 the past 20,000 years (Fig. 1). The consistency between these independent, but complementary
87 proxies constitutes a robust record of past climate changes and suggests that there are strong
88 linkages between changes in large-scale convection, extreme precipitation, and ecology. More
89 arid conditions occur during the late glacial (ca. 20-15 kyr BP), with higher $\delta^{13}\text{C}_{\text{OM}}$ values (-8 to
90 -10‰), indicating a C₄ grass-dominated landscape and more positive $\delta\text{D}_{\text{wax}}$ values and low %Ti
91 suggesting reduced MCS activity. At ca. 14.5 kyr BP, all three proxies change abruptly,
92 reflecting a rapid increase in MCS activity and the establishment of overall wetter conditions.
93 This initial deglacial intensification of MCS activity is terminated by a gradual return to drier,
94 less stormy conditions which peaked in the early to mid-Holocene (5-7 kyr BP). Wetter
95 conditions and greater MCS activity return gradually in the late Holocene. Although the gradual
96 nature and timing of Holocene climate changes suggests a response to orbitally-driven changes
97 in solar insolation, superimposed on these gradual changes are coherent millennial-scale arid
98 events that are synchronous with the cold phases of North Atlantic "Bond Events" 1, 2, 3, 4, 5, 7
99 and 8, suggesting a link to climate changes in the North Atlantic on millennial timescales
100 (Supplementary Fig. 4)¹³.

101

102 To better understand the controls on these hydroclimatic changes, we compare the proxy
103 reconstructions from Hall's Cave against the TraCE-21ka simulation of climate over the past
104 21,000 years ¹⁴. This simulation, conducted using the Community Climate System Model version
105 3 (CCSM3) of the U.S. National Center for Atmospheric Research, includes changes in global
106 climate driven by changes in greenhouse gas concentrations, orbital insolation, and
107 waning/collapsing continental ice sheets, including their effect on coastlines via changes in sea
108 level, as well as fresh water fluxes into the ocean ¹⁴. Because the climate model used in this
109 simulation inadequately represents MCS activity due to its coarse atmospheric resolution
110 ($\sim 3.75^\circ$), here we explore changes in the large-scale dynamics favoring the development of warm
111 season convective activity (i.e., the springtime LLJ and the latitudinal position of mid-
112 tropospheric baroclinicity) ¹, rather than precipitation. We focus on the spring (March to May)
113 because that is the time when the coupling between the LLJ and frontal systems associated with
114 mid-latitude baroclinic waves is strongest, producing frequent and intense precipitation
115 associated with MCSs ¹. To do so, we define an index of LLJ intensity, quantified as the
116 southerly wind at 850 hPa level averaged over the 95-103°W, 22-34°N domain containing the
117 Hall's Cave site and also where the maximum southerly flow occurs in the model (see
118 Supplementary Information for details). We use this index to diagnose the drivers of past MCS
119 variability because, in addition to being a metric of the large scale conditions favoring
120 convective activity in this region, the climate model used in the TraCE-21ka simulation
121 realistically reproduces the seasonal development of the southerly LLJ and its spatial extent
122 under current conditions.

123

124 The temporal evolution of the simulated LLJ intensity shows striking similarities to our multi-
125 proxy reconstructions of past MCS activity and vegetation change from Hall's Cave, including a
126 weaker-than-present springtime LLJ at the LGM, an abrupt intensification starting at around 13.9
127 kyr BP, a subsequent gradual weakening of the LLJ during the early to mid-Holocene and a
128 gradual strengthening of the LLJ after ca. 5 kyr BP (Fig 1). During the LGM, the North
129 American ice sheets expanded, cooling the continental interior and leading to the development of
130 anomalous high-pressure over the central U.S. This weakens the zonal pressure gradient between
131 the central US and the Atlantic, reducing the strength of the geostrophic LLJ winds and causing
132 the LLJ to turn eastward (Supplementary Fig. 7). Given the strong dynamical control of the LLJ
133 on MCS development in this region, this should result in weaker or less frequent storms,
134 consistent with the δD and %Ti data from Hall's Cave. Although reduced rainfall and storm
135 activity during the LGM could also occur because of the thermodynamic effects associated with
136 an ice-sheet driven southward displacement of the wintertime jet stream¹⁵⁻¹⁹, which ventilates
137 cold dry air into the region^{20,21}, this response should also strengthen the baroclinic forcing over
138 the southern Great Plains, making conditions more favorable for MCS genesis. Thus, a
139 dynamical control of MCS variability via changes in LLJ intensity, driven primarily by
140 continental land surface temperatures is the more likely explanation for weaker MCS activity and
141 more arid conditions during the LGM than a thermodynamic forcing associated with ventilation.

142

143 The simulated deglacial intensification of the LLJ is remarkably similar to the rapid increase in
144 MCS activity and the expansion of C₃ vegetation reconstructed from Hall's Cave (Fig. 1). In the
145 model, strengthening of the LLJ at this time is caused by the enhancement of the zonal pressure
146 gradient across central North America due to a combination of land surface warming and remote

147 forcing of the North Atlantic Subtropical High (NASH). Laurentide Ice Sheet collapse results in
148 land surface warming and the development of anomalous low pressure along the southern margin
149 of the ice sheet, across the northern Great Plains and the Great Lakes region, largely as a result of
150 changes in land surface albedo (Fig. 2a; Supplementary Fig. 9). At the same time, the NASH
151 strengthens as a result of topographic forcing associated with the Laurentide ice sheet collapse
152 (Fig. 2a)²²⁻²⁴. Together, these responses steepen the zonal pressure gradient, intensifying the
153 geostrophic LLJ (Fig. 2a). This suggests that as the ice sheet retreats, the LLJ responds
154 dynamically by strengthening in response to land surface warming over the Great Plains. Proxy
155 hydroclimate and vegetation records from across central U.S. show a similar abrupt change at
156 this time²⁵⁻²⁸ (Fig. 2c; Supplementary Information), supporting the hypothesis that this event
157 reflects a change in regional atmospheric dynamics associated with the deglacial intensification
158 of the LLJ.

159

160 In the TraCE-21ka simulation, this transition initiates at 13.9 kyr BP, in conjunction with the
161 separation of the Cordilleran and Laurentide ice sheets²⁹. We note that the abrupt change in the
162 proxy records occurs slightly earlier than in the model (ca. 14.5 kyr BP at Hall's Cave).

163 However, the earlier timing in the proxy records is consistent with updated estimates from North
164 American deglacial chronologies³⁰ which indicate that the separation occurred at about 14.1-
165 14.6 kyr BP and that the ice sheet changes were prescribed too late in the transient simulations
166 (see Supplementary Information). Support for the dominant role of ice collapse in driving this
167 response, rather than global climate changes associated with the Bølling-Allerød warming (14.9
168 kyr BP), is from the TraCE-21ka single-forcing experiments, which show the same behavior in
169 ice sheet-only simulations (Supplementary Information).

170

171 Following initial strengthening of the LLJ associated with ice sheet collapse and progressing into
172 the Holocene, land surface temperature changes driven by gradual changes in northern
173 hemisphere insolation modulates the intensity of the LLJ. After the initial strengthening at 13.9
174 kyr BP, the simulated LLJ decreases gradually from ca. 12 kyr BP to the mid Holocene (ca. 5-7
175 kyr BP) and then increases towards the present following changes in spring insolation (Fig. 3a).
176 In the model, decreased early- to mid-Holocene insolation cools the land surface relative to the
177 ocean, increasing surface pressure over the southern Rockies and central Great Plains and
178 weakening the LLJ. As spring insolation gradually increases towards the late-Holocene (i.e., 5-0
179 kyr BP), warming of the land surface strengthens the springtime LLJ (Fig. 3b).

180

181 Support for springtime insolation changes as the dominant driver of Holocene changes in the LLJ
182 comes from the strong agreement between the timing of changes in proxy-reconstructed MCS
183 activity, spring insolation and the associated changes in springtime LLJ activity in TraCE-21ka
184 (Fig. 3a). In contrast, summer or integrated warm-season insolation changes peak earlier and
185 produce a stronger LLJ in the early to mid-Holocene, inconsistent with the observed changes in
186 hydroclimate and MCS activity evident at Hall's Cave. Additional support comes from modern
187 observations; while the LLJ responds to land surface warming and the development of zonal
188 pressure gradient anomalies seasonally, MCS activity is predominantly associated with
189 springtime land surface conditions because little rainfall occurs in the summer when weak large-
190 scale baroclinicity is unfavorable for MCS genesis, irrespective of the strength of the LLJ¹. In
191 fact, this mechanism, whereby springtime land surface warming is critical for seasonal changes
192 in LLJ intensity, is evident across mid-Holocene climate simulations performed as part of the

193 Paleoclimate Modeling Intercomparison Project (PMIP3) ³¹ and explains drier mid-Holocene
194 conditions in the central US at that time ³²⁻³⁶, despite the maxima in summertime insolation
195 (Supplementary Fig. 10).

196

197 Although model-inferred changes in LLJ strength during the Holocene are similar in timing to
198 reconstructed changes in vegetation and MCS activity, the δD_{wax} record suggests more dramatic
199 changes in MCS activity compared with model-inferred changes in the LLJ (Fig. 1). Given the
200 evidence presented here for a dominant land surface temperature control over LLJ strength
201 throughout the last 20 kyr, we hypothesize that the model-proxy discrepancy may be the result of
202 land surface feedbacks. During the early Holocene, drought tolerant C₄ summer grasses occupied
203 nearly all (~90%) of the landscape (Fig. 1) ³³, and was likely associated with a significant
204 reduction in evapotranspiration, locally reducing land-atmosphere latent heat and moisture fluxes
205 and further inhibiting MCS development. Such land surface feedbacks are known to play an
206 important role in modulating warm season temperature and precipitation on interannual scales
207 today ³⁷⁻³⁹, though they are not sufficiently represented in the current generation of general
208 circulation models ⁴⁰. The Great Plains have been identified as one of the most significant
209 vegetation “hotspots” for future change ⁴¹, a prediction consistent with the dramatic vegetation
210 changes observed in the Hall’s Cave record. Underestimating these changes may influence
211 patterns of land surface warming with impacts on the magnitudes of changes in both the large-
212 scale atmospheric dynamics and precipitation.

213

214 The paleoclimatic reconstruction from Hall’s Cave provides robust evidence for a highly
215 sensitive climate system in the central U.S. dominated by changes in springtime MCSs. The

216 similarities between proxy reconstructions of MCS behavior and vegetation reconstructed from
217 $\delta^{13}\text{C}$ further suggests that these changes in convective storm development also drive large-scale
218 ecosystem changes. While state-of-the-art climate models are unable to accurately represent
219 storm systems such as MCSs, the remarkable similarities between changes in proxy-
220 reconstructed MCS behavior and climate model simulations of the springtime LLJ supports that
221 dominant dynamical control of the seasonal changes in LLJ strength on the development of
222 convective storms over the Great Plains over the last 20 kyr. Changes in the LLJ are forced by
223 springtime land surface temperature changes over the central Great Plains, consistent with
224 observed increases in LLJ strength and MCS activity in response to global warming over the past
225 three decades ⁴. Our reconstruction indicates that this mechanism has dominated the response of
226 the great plains hydroclimate system for the last 20 kyr, and will lead to an increased risk of
227 extreme weather in response to future warming. However, the results of this study also suggest
228 that models may underestimate the magnitude and rate of future changes in MCS activity in
229 response to land surface warming because of land surface-vegetation feedbacks on the
230 development of these systems.

231

232

233 **Methods**

234 1. Paleoclimate reconstructions

235 Geochemical paleoclimate reconstructions were generated from new sediment cores taken from
236 Hall's Cave. Chronological control for the cave sediment record is based on 37 previously
237 published AMS ^{14}C measurements made primarily on collagen extracted from fossil bones
238 preserved in the cave sediments (Supplementary Table 1). Age-depth modeling was performed
239 using the Bayesian age-depth modeling R-program BACON ⁴² and the IntCal13 radiocarbon
240 calibration curve ⁴³ (see Supplementary Information for more details).

241

242 The cores were sampled every 1 cm to generate high-resolution continuous records of $\delta\text{D}_{\text{wax}}$ and
243 $\delta^{13}\text{C}_{\text{OM}}$. Approximately 2-20 mg of freeze-dried and homogenized bulk sediment samples were
244 used for $\delta^{13}\text{C}_{\text{OM}}$ analysis on an elemental analyzer (Costech Instruments Elemental Combustion
245 System 4010) coupled to an isotope ratio mass spectrometer (Thermo Scientific Delta V Plus).
246 For compound-specific $\delta\text{D}_{\text{wax}}$ analysis, approximately 20-50 g of freeze-dried and homogenized
247 samples were extracted using microwave solvent extraction (CEM MARS) with dichloromethane
248 : methanol (9:1; v/v). Polar and nonpolar fractions were separated using silica gel
249 chromatography with hexane and dichloromethane : methanol (9:1; v/v). The nonpolar fraction
250 containing n-alkanes were further treated with urea adduction, which is then used for $\delta\text{D}_{\text{wax}}$
251 analysis on a TRACE gas chromatograph equipped with a DB-5ms column (30 m \times 0.25 μm \times
252 0.25 mm), coupled to a Delta V isotope ratio mass spectrometer via a pyrolysis interface
253 operated at 1430°C. The $\delta\text{D}_{\text{wax}}$ values reported in this paper is based on C_{27} n-alkane, which
254 shows the greatest abundance and best chromatography, and is corrected for local vegetation
255 change and global ice volume. For additional technical details, see Supplementary Information.

256

257 The %Ti abundance record was generated by energy-dispersive x-ray fluorescence (ED-XRF).
258 Using a Niton FXL 950 portable XRF analyzer equipped with an Ag x-ray tube. The cores were
259 sampled every 5 mm, and the subsamples were dried at 50°C, sieved to remove the > 0.5 mm
260 fraction, homogenized with an agate mortar and pestle, and hand-pressed to a uniform density
261 prior to analysis. Each sample was analyzed for 60 seconds in triplicate (see Supplementary
262 Information for more details).

263

264 For the carbon isotope measurements on bulk organic matter, the core was sampled every 1 cm.
265 2-20 mg freeze-dried, homogenized samples were weighed into silver capsules and acidified
266 with sulfurous acid to remove inorganic carbon ⁴⁴. Carbon isotope analysis was performed by
267 combustion in an elemental analyzer (Costech Instruments Elemental Combustion System 4010)
268 coupled to an isotope ratio mass spectrometer (Thermo Scientific Delta V Plus). The analytical
269 precision of these analyses was 0.24‰ based on repeated measurements of an in-house standard.

270

271 2. Climate model experiments

272 We analyzed the model output of the Transient Climate Simulations of the Last 21,000 Years
273 experiment ¹⁴, performed with the fully coupled Community Climate System Model version 3
274 (CCSM3) at the National Center for Atmospheric Research (NCAR). The atmospheric data was
275 downloaded from the Climate Data Gateway at NCAR (<https://www.earthsystemgrid.org/>).
276 TraCE-21ka was simulated with time-evolving external forcings including orbital parameters,
277 concentrations of greenhouse gases, continental ice sheets and meltwater fluxes. In addition to
278 the full TraCE-21ka simulation, we also analyzed the model output from the single-forcing

279 experiments of TraCE-21ka, where only one of the external forcing (i.e., ice sheet volume,
280 greenhouse gas, insolation, meltwater flux) was prescribed to change as in the full simulation,
281 whereas the rest of these parameters were kept at their LGM levels. Lastly, we used the mid-
282 Holocene (6 ka) and pre-Industrial (0 ka) experiments available through the Paleoclimate
283 Modeling Intercomparison Project (PMIP3)³¹. These PMIP3 simulations share a common
284 PMIP3 protocol for boundary conditions and use interactive carbon cycle. The vegetation and
285 land surface are either computed using a dynamical vegetation module or prescribed as in pre-
286 Industrial. More details are provided in Supplementary Information.

287

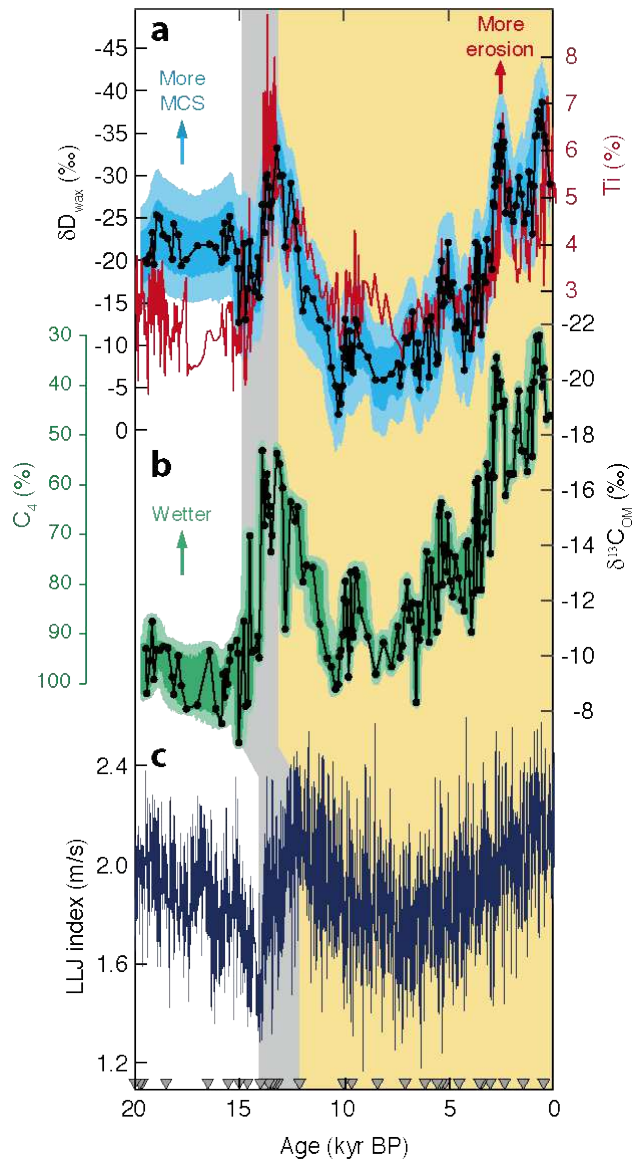
288 **Acknowledgments:** We thank C. Bell and E. Lundelius for discussions and T. Wicks for
289 assistance in fieldwork and data analysis. We thank TD Hall and B Hall of Hall’s Ranch for
290 access to the site. **Funding:** T.M.S. received partial support for this work from the National
291 Science Foundation AGS1702271 and from a UT system-CONACYT collaborative research
292 grants (ConTex grant no. 2017-33).

293
294 **Author contributions:** T.M.S., N.P.M. and P.R. designed the study. T.M.S. facilitated and
295 conducted the fieldwork. T.M.S. and C.S. conducted the laboratory work and analyzed the data.
296 C.S., P.D.N and N.P.M analyzed the climate model output. T.M.S., C.S. and P.D.N conducted
297 the data-model analysis. T.M.S. and C. S. wrote the paper. C.S. created the figures. All authors
298 contributed to editing the final version of the manuscript.

299
300 **Competing interests:** Authors declare no competing interests.

301
302 **Data and materials availability:** Data associated with this article are available for download
303 from the National Oceanic and Atmospheric Administration National Centers for Environmental
304 Information Paleoclimatology archive (www.ncdc.noaa.gov/paleo). Additional data related to
305 this paper may be requested from the authors.

306



307

308 **Fig. 1. Proxy and model estimates of hydroclimate variations in the southern Great Plains.**

309 (a) Records of δD_{wax} and %Ti at Hall's Cave, interpreted as changes in MCS and soil erosion

310 from intense precipitation, respectively. δD_{wax} is corrected for vegetation and ice volume

311 (Supplementary Information). (b) $\delta^{13}C_{TOC}$ at Hall's Cave, interpreted as changes in the relative

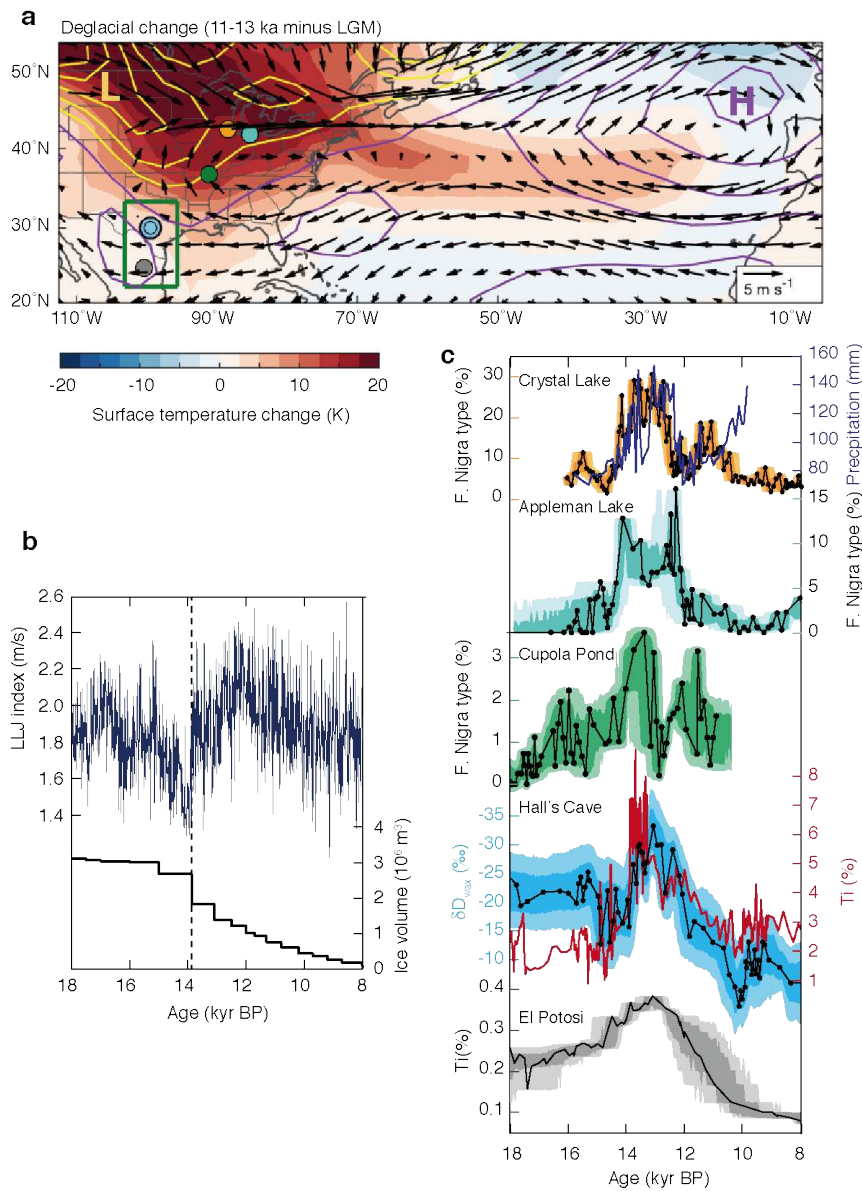
312 abundance of C_3 and C_4 vegetation. (c) Springtime Low-Level Jet (LLJ) index in TraCE-21ka.

313 Shadings on the reconstructions reflect 1 σ (dark) and 2 σ (light) uncertainties. Triangles denote

314 radiocarbon dates. Grey and yellow regions reflect ice sheet and insolation-dominated intervals,

315 respectively. The timing of the largest ice volume change in TraCE-21ka was prescribed at 13.9
316 ka to match other boundary condition changes, trailing the estimates from updated deglacial
317 chronologies (see Supplementary Information for details).

318



319

320 **Fig. 2. Deglacial hydroclimate change associated with ice sheet “saddle collapse”. (a)**

321 Changes in springtime (March to May) surface air temperature (shadings), sea-level pressure

322 (contours; yellow: negative values; purple: positive values), and 850 hPa winds (vectors) during

323 11-13 ka relative to the LGM, showing strong warming over North America continent, steepened

324 zonal pressure gradient, and intensified LLJ. Colored dots indicate site locations of the

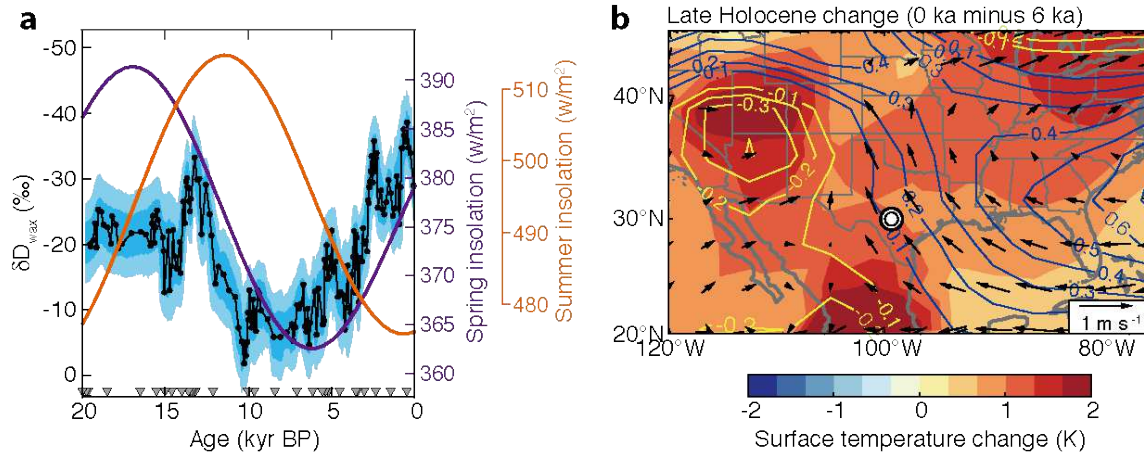
325 paleoclimate records shown in panel (c). The green rectangle indicates the area used to define the

326 LLJ index. **(b)** Simulated changes in the springtime LLJ and prescribed changes in the North
327 American Ice Sheets in TraCE-21ka, showing that the LLJ intensification is synchronous with
328 the largest drop in ice sheet volume. **(c)** Paleohydrologic records across the Great Plains showing
329 a deglacial hydrologic signal (see Supplementary Information for details). Shadings indicate 1σ
330 (dark) and 2σ (light) uncertainties based on analytical and age model errors.

331

332

333



334

335

336 **Fig. 3. Insolation-driven changes in hydroclimate during the Holocene. (a) Hall's Cave**

337 δD_{wax} and changes in spring (March 21st; purple) and summer (June 21st; orange) insolation at

338 30°N. (b) Changes in springtime surface temperature (shadings), sea-level pressure (contours;

339 yellow: negative values; blue: positive values; unit: mbar), and 850 hPa wind (vectors) during

340 the Late Holocene (0 ka minus 6 ka).

341

342

343

344 **References**

345

346 1 Feng, Z. *et al.* Spatiotemporal Characteristics and Large-Scale Environments of
347 Mesoscale Convective Systems East of the Rocky Mountains. *Journal of Climate* **32**,
348 7303-7328, doi:10.1175/jcli-d-19-0137.1 (2019).

349 2 Kousky, C. Informing climate adaptation: A review of the economic costs of natural
350 disasters. *Energy Economics* **46**, 576-592, doi:10.1016/j.eneco.2013.09.029 (2014).

351 3 Schumacher, R. S. & Johnson, R. H. Characteristics of U.S. Extreme Rain Events during
352 1999–2003. *Weather and Forecasting* **21**, 69-85, doi:10.1175/waf900.1 (2006).

353 4 Feng, Z. *et al.* More frequent intense and long-lived storms dominate the springtime trend
354 in central US rainfall. *Nature Communications* **7**, 13429, doi:10.1038/ncomms13429
355 (2016).

356 5 Maloney, E. D. *et al.* North American Climate in CMIP5 Experiments: Part III:
357 Assessment of Twenty-First-Century Projections*. *Journal of Climate* **27**, 2230-2270,
358 doi:10.1175/jcli-d-13-00273.1 (2014).

359 6 Cook, K. H., Vizy, E. K., Launer, Z. S. & Patricola, C. M. Springtime Intensification of
360 the Great Plains Low-Level Jet and Midwest Precipitation in GCM Simulations of the
361 Twenty-First Century. *Journal of Climate* **21**, 6321-6340, doi:10.1175/2008jcli2355.1
362 (2008).

363 7 Harding, K. J. & Snyder, P. K. Examining future changes in the character of Central U.S.
364 warm-season precipitation using dynamical downscaling. *Journal of Geophysical*
365 *Research: Atmospheres* **119**, 13,116-113,136, doi:10.1002/2014jd022575 (2014).

366 8 Christensen, J. H. *et al.* in *Climate Change 2013 the Physical Science Basis: Working*
367 *Group I Contribution to the Fifth Assessment Report of the Intergovernmental Panel on*
368 *Climate Change* 1217-1308 (Cambridge University Press, 2013).

369 9 Pfahl, S., O’Gorman, P. A. & Fischer, E. M. Understanding the regional pattern of
370 projected future changes in extreme precipitation. *Nature Climate Change* **7**, 423-427
371 (2017).

372 10 Sun, C., Shanahan, T. M. & Partin, J. Controls on the Isotopic Composition of
373 Precipitation in the South - Central United States. *Journal of Geophysical Research:*
374 *Atmospheres* **124**, 8320-8335, doi:10.1029/2018jd029306 (2019).

375 11 Sachse, D. *et al.* Molecular Paleohydrology: Interpreting the Hydrogen-Isotopic
376 Composition of Lipid Biomarkers from Photosynthesizing Organisms. *Annual Review of*
377 *Earth and Planetary Sciences* **40**, 221-249, doi:10.1146/annurev-earth-042711-105535
378 (2012).

379 12 Boutton, T. W., Archer, S. R., Midwood, A. J., Zitzer, S. F. & Bol, R. $\delta^{13}\text{C}$ values of soil
380 organic carbon and their use in documenting vegetation change in a subtropical savanna
381 ecosystem. *Geoderma* **82**, 5-41 (1998).

382 13 Bond, G. *et al.* Persistent solar influence on North Atlantic climate during the Holocene.
383 *Science* **294**, 2130-2136 (2001).

384 14 Liu, Z. *et al.* Transient Simulation of Last Deglaciation with a New Mechanism for
385 Bolling-Allerod Warming. *Science* **325**, 310-314, doi:10.1126/science.1171041 (2009).

386 15 Members, C. Climatic changes of the last 18,000 years: observations and model
387 simulations. *Science*, 1043-1052 (1988).

- 388 16 Oster, J. L., Ibarra, D. E., Winnick, M. J. & Maher, K. Steering of westerly storms over
389 western North America at the Last Glacial Maximum. *Nature Geoscience* **8**, 201-205,
390 doi:10.1038/ngeo2365 (2015).
- 391 17 Lora, J. M., Mitchell, J. L. & Tripathi, A. E. Abrupt reorganization of North Pacific and
392 western North American climate during the last deglaciation. *Geophysical Research*
393 *Letters* **43**, 11,796-711,804, doi:10.1002/2016gl071244 (2016).
- 394 18 Lora, J. M. Components and Mechanisms of Hydrologic Cycle Changes over North
395 America at the Last Glacial Maximum. *Journal of Climate* **31**, 7035-7051,
396 doi:10.1175/jcli-d-17-0544.1 (2018).
- 397 19 Conroy, J. L., Karamperidou, C., Grimley, D. A. & Guenther, W. R. Surface winds
398 across eastern and midcontinental North America during the Last Glacial Maximum: A
399 new data-model assessment. *Quaternary Science Reviews* **220**, 14-29,
400 doi:10.1016/j.quascirev.2019.07.003 (2019).
- 401 20 Bhattacharya, T., Tierney, J. E. & DiNezio, P. Glacial reduction of the North American
402 Monsoon via surface cooling and atmospheric ventilation. *Geophysical Research Letters*
403 **44**, 5113-5122, doi:10.1002/2017gl073632 (2017).
- 404 21 Chou, C. & Neelin, J. D. Mechanisms Limiting the Northward Extent of the Northern
405 Summer Monsoons over North America, Asia, and Africa*. *Journal of Climate* **16**, 406-
406 425, doi:10.1175/1520-0442(2003)016<0406:mltneo>2.0.co;2 (2003).
- 407 22 Cook, K. H. & Held, I. M. Stationary Waves of the Ice Age Climate. *Journal of Climate*
408 **1**, 807-819, doi:10.1175/1520-0442(1988)001<0807:swotia>2.0.co;2 (1988).
- 409 23 Löfverström, M., Caballero, R., Nilsson, J. & Kleman, J. Evolution of the large-scale
410 atmospheric circulation in response to changing ice sheets over the last glacial cycle.
411 *Climate of the Past* **10**, 1453-1471, doi:10.5194/cp-10-1453-2014 (2014).
- 412 24 Roberts, W. H. G., Li, C. & Valdes, P. J. The Mechanisms that Determine the Response
413 of the Northern Hemisphere's Stationary Waves to North American Ice Sheets. *Journal*
414 *of Climate* **32**, 3917-3940, doi:10.1175/jcli-d-18-0586.1 (2019).
- 415 25 Gonzales, L. M., Williams, J. W. & Grimm, E. C. Expanded response-surfaces: a new
416 method to reconstruct paleoclimates from fossil pollen assemblages that lack modern
417 analogues. *Quaternary Science Reviews* **28**, 3315-3332 (2009).
- 418 26 Gill, J. L., Williams, J. W., Jackson, S. T., Lininger, K. B. & Robinson, G. S. Pleistocene
419 megafaunal collapse, novel plant communities, and enhanced fire regimes in North
420 America. *Science* **326**, 1100-1103 (2009).
- 421 27 Jones, R. A., Williams, J. W. & Jackson, S. T. Vegetation history since the last glacial
422 maximum in the Ozark highlands (USA): A new record from Cupola Pond, Missouri.
423 *Quaternary Science Reviews* **170**, 174-187 (2017).
- 424 28 Roy, P. D. *et al.* Atlantic Ocean modulated hydroclimate of the subtropical northeastern
425 Mexico since the last glacial maximum and comparison with the southern US. *Earth and*
426 *Planetary Science Letters* **434**, 141-150 (2016).
- 427 29 Gregoire, L. J., Payne, A. J. & Valdes, P. J. Deglacial rapid sea level rises caused by ice-
428 sheet saddle collapses. *Nature* **487**, 219-222, doi:10.1038/nature11257 (2012).
- 429 30 Tarasov, L., Dyke, A. S., Neal, R. M. & Peltier, W. R. A data-calibrated distribution of
430 deglacial chronologies for the North American ice complex from glaciological modeling.
431 *Earth and Planetary Science Letters* **315-316**, 30-40, doi:10.1016/j.epsl.2011.09.010
432 (2012).

433 31 Braconnot, P. *et al.* Evaluation of climate models using palaeoclimatic data. *Nature*
434 *Climate Change* **2**, 417-424, doi:10.1038/nclimate1456 (2012).

435 32 Nordt, L., Von Fischer, J., Tieszen, L. & Tubbs, J. Coherent changes in relative C4 plant
436 productivity and climate during the late Quaternary in the North American Great Plains.
437 *Quaternary Science Reviews* **27**, 1600-1611, doi:10.1016/j.quascirev.2008.05.008 (2008).

438 33 Cordova, C. E. & Johnson, W. C. An 18 ka to present pollen- and phytolith-based
439 vegetation reconstruction from Hall's Cave, south-central Texas, USA. *Quaternary*
440 *Research* **92**, 497-518, doi:10.1017/qua.2019.17 (2019).

441 34 Williams, J. W., Shuman, B., Bartlein, P. J., Diffenbaugh, N. S. & Webb III, T. Rapid,
442 time-transgressive, and variable responses to early Holocene midcontinental drying in
443 North America. *Geology* **38**, 135-138 (2010).

444 35 Shuman, B. N. & Marsicek, J. The structure of Holocene climate change in mid-latitude
445 North America. *Quaternary Science Reviews* **141**, 38-51 (2016).

446 36 Skinner, C. B., Lora, J. M., Payne, A. E. & Poulsen, C. J. Atmospheric river changes
447 shaped mid-latitude hydroclimate since the mid-Holocene. *Earth and Planetary Science*
448 *Letters* **541**, 116293 (2020).

449 37 Koster, R. D. Regions of Strong Coupling Between Soil Moisture and Precipitation.
450 *Science* **305**, 1138-1140, doi:10.1126/science.1100217 (2004).

451 38 Dirmeyer, P. A. The terrestrial segment of soil moisture–climate coupling. *Geophysical*
452 *Research Letters* **38** (2011).

453 39 Al-Yaari, A., Ducharne, A., Cheruy, F., Crow, W. T. & Wigneron, J. P. Satellite-based
454 soil moisture provides missing link between summertime precipitation and surface
455 temperature biases in CMIP5 simulations over conterminous United States. *Sci Rep* **9**,
456 1657, doi:10.1038/s41598-018-38309-5 (2019).

457 40 Jiang, X., Niu, G.-Y. & Yang, Z.-L. Impacts of vegetation and groundwater dynamics on
458 warm season precipitation over the Central United States. *Journal of Geophysical*
459 *Research* **114**, doi:10.1029/2008jd010756 (2009).

460 41 Hufkens, K. *et al.* Productivity of North American grasslands is increased under future
461 climate scenarios despite rising aridity. *Nature Climate Change* **6**, 710-714,
462 doi:10.1038/nclimate2942 (2016).

463 42 Blaauw, M. & Christen, J. A. Flexible paleoclimate age-depth models using an
464 autoregressive gamma process. *Bayesian analysis* **6**, 457-474 (2011).

465 43 Reimer, P. J. *et al.* Selection and treatment of data for radiocarbon calibration: an update
466 to the International Calibration (IntCal) criteria. *Radiocarbon* **55**, 1923-1945 (2013).

467 44 Fernandes, M. & Krull, E. How does acid treatment to remove carbonates affect the
468 isotopic and elemental composition of soils and sediments? *Environmental Chemistry* **5**,
469 33-39 (2008).

470

Figures

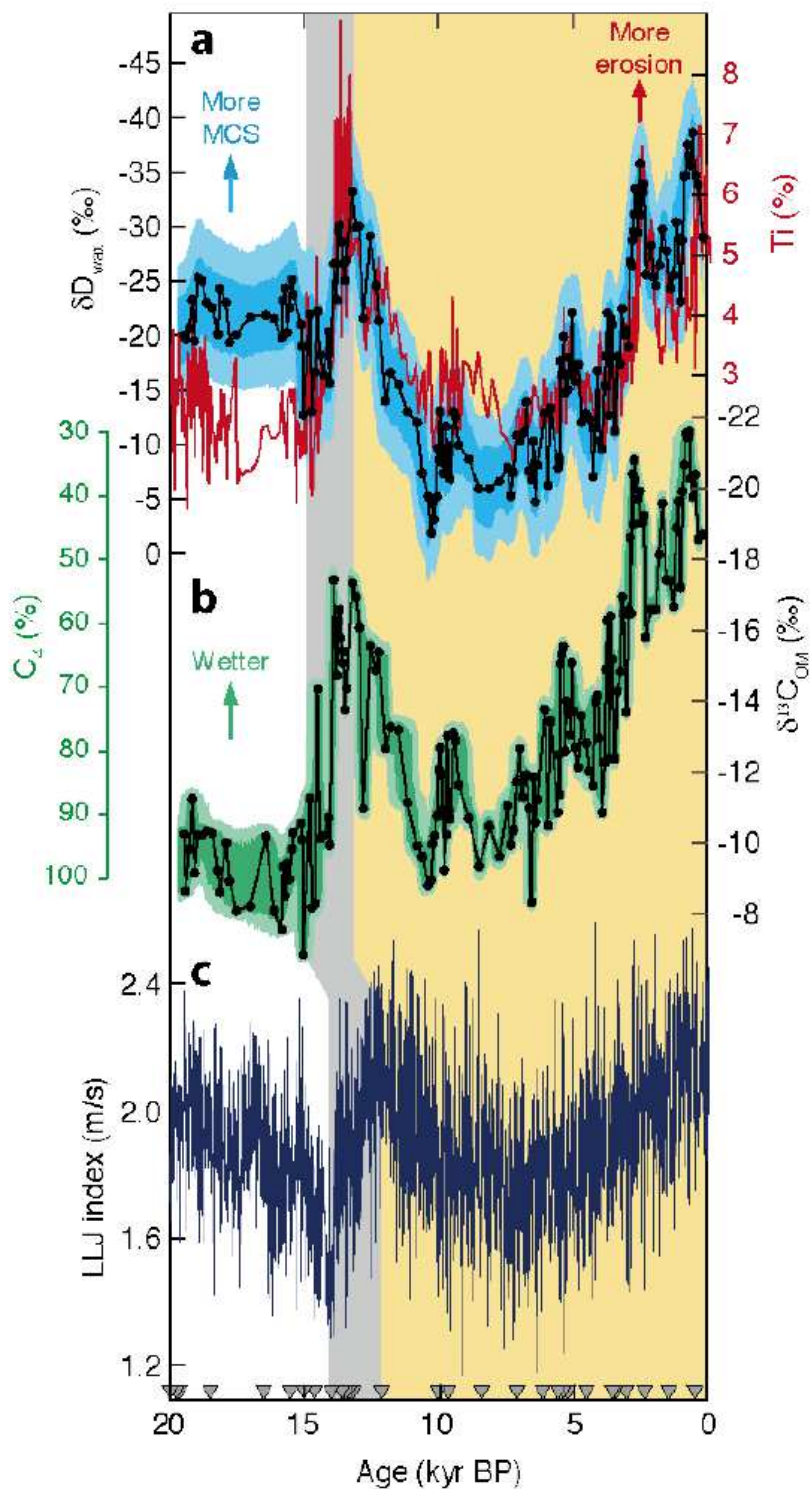


Figure 1

Proxy and model estimates of hydroclimate variations in the southern Great Plains. (a) Records of dD_{wax} and %Ti at Hall's Cave, interpreted as changes in MCS and soil erosion from intense precipitation, respectively. dD_{wax} is corrected for vegetation and ice volume (Supplementary Information). (b)

d13CTOC at Hall's Cave, interpreted as changes in the relative abundance of C3 and C4 vegetation. (c) Springtime Low-Level Jet (LLJ) index in TraCE-21ka. Shadings on the reconstructions reflect 1s (dark) and 2s (light) uncertainties. Triangles denote radiocarbon dates. Grey and yellow regions reflect ice sheet and insolation-dominated intervals, respectively. The timing of the largest ice volume change in TraCE-21ka was prescribed at 13.9 ka to match other boundary condition changes, trailing the estimates from updated deglacial chronologies (see Supplementary Information for details).

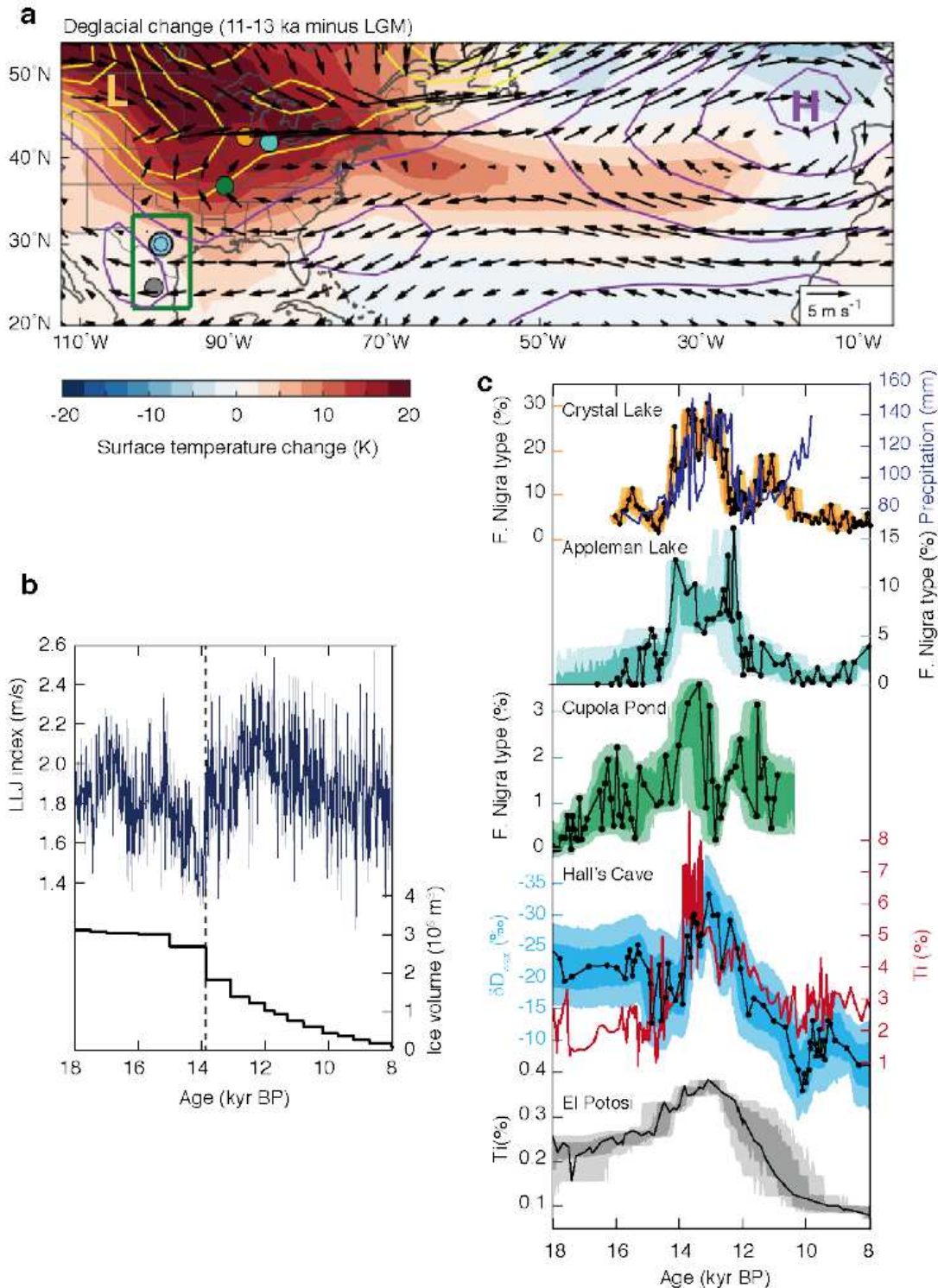


Figure 2

Deglacial hydroclimate change associated with ice sheet “saddle collapse”. (a) Changes in springtime (March to May) surface air temperature (shadings), sea-level pressure (contours; yellow: negative values; purple: positive values), and 850 hPa winds (vectors) during 11-13 ka relative to the LGM, showing strong warming over North America continent, steepened zonal pressure gradient, and intensified LLJ. Colored dots indicate site locations of the paleoclimate records shown in panel (c). The green rectangle indicates the area used to define the LLJ index. (b) Simulated changes in the springtime LLJ and prescribed changes in the North American Ice Sheets in TraCE-21ka, showing that the LLJ intensification is synchronous with the largest drop in ice sheet volume. (c) Paleohydrologic records across the Great Plains showing a deglacial hydrologic signal (see Supplementary Information for details). Shadings indicate 1s (dark) and 2s (light) uncertainties based on analytical and age model errors.

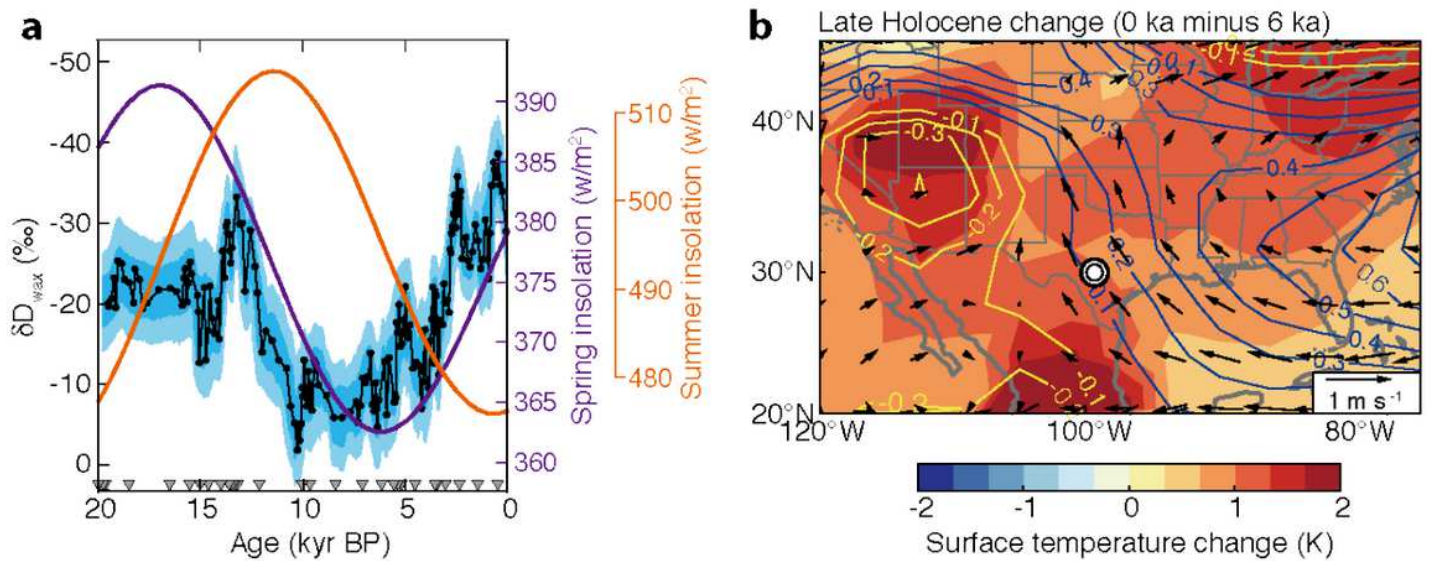


Figure 3

Insolation-driven changes in hydroclimate during the Holocene. (a) Hall’s Cave δD_{wax} and changes in spring (March 21st; purple) and summer (June 21st; orange) insolation at 30°N. (b) Changes in springtime surface temperature (shadings), sea-level pressure (contours; yellow: negative values; blue: positive values; unit: mbar), and 850 hPa wind (vectors) during the Late Holocene (0 ka minus 6 ka).

Supplementary Files

This is a list of supplementary files associated with this preprint. Click to download.

- [HallsCaveSOM.pdf](#)
- [supplementarydataS1.xlsx](#)